Analytical, One-Dimensional, and Axisymmetric Finite Element Modeling of Steel-Fiber Pullout

Paulo Victor Sales de Souza   Eduardo Carneiro Daniel

Escola Politécnica, University of São Paulo, São Paulo, Brazil

Abstract

This study investigates the fully bonded pullout of a straight steel fiber through three models of increasing dimensional complexity. The closed-form shear-lag benchmark is taken from Zhan and Meschke. A one-dimensional finite element formulation is derived from the weak form using linear elements and consistent distributed-interface stiffness, while a two-dimensional axisymmetric Abaqus model represents fiber and matrix explicitly with CAX4 elements. The custom code passes analytical, equilibrium, symmetry, energy, and convergence checks. Its 80-element pullout-force error is 0.033%, a code-verification result because the closed-form and discrete models solve the same boundary-value problem. The observed rates approach second order for reaction and displacement and first order for derivative and energy quantities. Independent axial and radial studies satisfy the adopted 0.5% criterion; the practical 984-node axisymmetric reference is 14.6% stiffer than the shear-lag model, a model-form discrepancy within the accessible refinement range. At the bonded limit, the analytical and one-dimensional results coincide with the digitized experimental estimate to its defensible graphical precision, whereas the axisymmetric result is about 14.7% higher. The hierarchy separates code verification, mesh sensitivity, and limited benchmark reproduction.

Keywords: steel-fiber pullout; shear-lag; finite element method; mesh convergence; axisymmetric analysis; code verification.

1 Introduction

Steel fibers improve the post-cracking response of cementitious composites by transferring forces across cracks. At the scale of one fiber, this mechanism is characterized by the pullout force versus end-displacement relation, which provides a basic constituent for macroscopic crack-bridging models [1]. Experimental, analytical, and numerical studies show that the response depends on fiber geometry, inclination, matrix properties, and the fiber-matrix interaction [2]. Discrete representations of individual fibers are particularly useful when the spatial distribution of load transfer or the interaction with matrix cracking is relevant [3, 4]. At the composite scale, fiber orientation, distribution, and group effects introduce additional mechanisms that cannot be inferred from a single-fiber test alone [5].

For a straight fiber aligned with the loading direction, Zhan and Meschke [1] divide pullout into three regimes. In the *bonded state*, the interface remains intact and its shear response is linear. In the *debonding stage*, damage progressively propagates from the loaded end. After complete debonding, the fiber slides through its channel and residual friction governs the *pulling-out phase*. The first regime is deceptively simple: it is linear, but the axial force is strongly nonuniform because load is transferred continuously from the fiber to the surrounding matrix.

The objective of this work is to examine that bonded regime with a controlled hierarchy of models. Model A is the published shear-lag solution and defines the exact reference for the adopted one-dimensional boundary-value problem. Model B is a custom finite element implementation derived from its weak form. Model C is an axisymmetric continuum model in which the matrix deformation is resolved explicitly. The comparison is designed to answer three distinct questions: whether the custom code solves its governing equations correctly, whether the numerical responses are mesh-converged, and how the modeling assumptions affect agreement with the published experiment. These questions are deliberately separated because agreement between Models A and B verifies an implementation, but does not constitute independent physical validation.

2 Benchmark and modeling scope

The benchmark is the straight, non-inclined fiber analyzed by Zhan and Meschke [1]. A circular steel fiber of radius r_f and embedded length L is centered in a cylindrical matrix of radius R. The coordinate x starts at the embedded tip and ends at the loaded matrix surface. The applied quantity is the axial end displacement $\delta = u(L)$; the pullout force F is recovered as a reaction. Figure 1 summarizes the geometry and boundary conditions used in the reduced and continuum models.

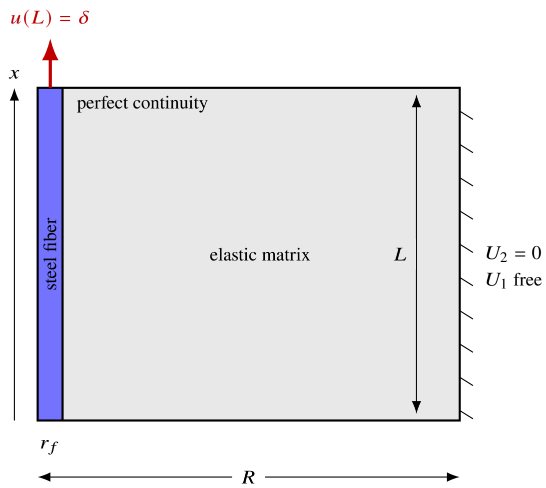

Figure 1: Axisymmetric meridional domain and loading. In the one-dimensional model, the matrix is condensed into a distributed shear stiffness; in the continuum model, the two material regions share the partition at $r = r_f$.

The published material, geometric, and interaction parameters are listed in Table 1. Calculations use the consistent N-mm-MPa unit system. The fiber area and perimeter are $A_f = \pi d_f^2/4$ and $p_f = \pi d_f$, respectively. The ratio R/r_f is dimensionless. In Models A and B, ν_f plays no role because the fiber is treated as a uniaxial bar; it enters only the axisymmetric continuum response of Model C. The fiber yield stress is retained as an a posteriori check. The residual friction $\tau_0 = 0.64$ MPa and reference slip $s_{\text{ref}} = 0.25$ mm reported in Ref. [1] govern later stages and are therefore not activated here.

Table 1: Benchmark parameters from Zhan and Meschke [1].

Quantity	Value	Quantity	Value
E_m	31,513 MPa	ν_m	0.20
E_f	210,000 MPa	ν_f	0.30
f_y	275 MPa	d_f	0.50 mm
L	10.0 mm	R/r_f	50.8
$\tau_{\max}$	3.18 MPa	R	12.7 mm

Table 2 makes explicit which physical fields are retained by each model and, consequently, what can legitimately be inferred from each comparison.

Table 2: Model hierarchy and role in the study.

Model	Representation	Primary role
A	Closed form; matrix condensed into G	Exact shear-lag reference
B	1D FE; distributed bond stiffness	Custom-code verification
C	CAX4 fiber–matrix continua	Model-form comparison

3 Analytical shear-lag model

3.1 Physical meaning and governing equations

The shear-lag concept describes a spatial delay in axial load transfer, not a time delay. When the exposed end is pulled, axial deformation is largest near that end. Interfacial shear progressively transfers force from the fiber to the matrix, so the fiber axial force decreases toward the embedded tip. The matrix is represented by a distributed elastic restraint rather than by an axially uniform reaction.

In the bonded regime, the relative displacement $u(x)$ and the interfacial shear stress are related by [1]

$$\tau(x) = Gu(x), \qquad G = \frac{E_m}{d_f(1+\nu_m)\ln(R/r_f)}. \tag{1}$$

The quantity G has units of stress per unit displacement (MPa/mm); it is a *relative bond modulus*, not the conventional shear modulus of the matrix. It condenses the radial distribution of matrix shear deformation between r_f and R into a one-dimensional relation. Here $u(x)$ is the fiber-axis displacement relative to the axially fixed matrix boundary at $r = R$, not a local jump across the perfectly bonded interface. This definition permits $u'(x)$ to represent the fiber axial strain in Eq. (2).

Equilibrium and axial compatibility of a differential fiber segment give

$$\frac{\mathrm{d}N}{\mathrm{d}x} = p_f\tau, \qquad N = E_fA_f\frac{\mathrm{d}u}{\mathrm{d}x}. \tag{2}$$

For constant properties, Eqs. (1)–(2) lead to

$$E_fA_fu'' - p_fGu = 0, \qquad \lambda^2 = \frac{p_fG}{E_fA_f}, \tag{3}$$

with $N(0) = 0$ at the embedded tip and $u(L) = \delta$ at the loaded end.

3.2 Closed-form solution and bonded limit

The solution written in terms of the prescribed displacement is

$$u(x) = \delta\frac{\cosh(\lambda x)}{\cosh(\lambda L)}, \tag{4}$$

$$N(x) = E_fA_f\lambda\delta\frac{\sinh(\lambda x)}{\cosh(\lambda L)}, \tag{5}$$

$$\tau(x) = Gu(x), \tag{6}$$

$$F(\delta) = N(L) = E_fA_f\lambda\tanh(\lambda L)\,\delta. \tag{7}$$

The inverse of λ is a characteristic transfer length: over distances of a few $1/\lambda$ from the loaded end, most of the axial load is transferred to the matrix. For the benchmark,

$$G = 13371.449 \text{ MPa/mm},$$
$$\lambda = 0.713715 \text{ mm}^{-1}, \qquad \lambda^{-1} = 1.40112 \text{ mm}. \tag{8}$$

Because $u(x)$ and $\tau(x)$ increase monotonically, the maximum interfacial stress occurs at $x = L$. The fully bonded regime ends when

$$s_0 = \frac{\tau_{\max}}{G} = 2.378201\times10^{-4} \text{ mm}. \tag{9}$$

At this displacement, the analytical stiffness and force are

$$K_{\text{ref}} = 29428.845 \text{ N/mm}, \qquad F_0 = K_{\text{ref}}s_0 = 6.998772 \text{ N}. \tag{10}$$

The corresponding maximum fiber stress is 35.644 MPa, only 12.96% of the reported yield stress. The elastic-fiber assumption is consequently consistent within the modeled interval. Equation (9) marks the *initiation* of debonding; it is not the maximum force of the complete experimental pullout curve.

4 One-dimensional FE formulation

4.1 Weak form and element equations

Let w be a virtual displacement satisfying $w(L) = 0$. Multiplication of Eq. (3) by w, integration by parts, and use of the natural condition $N(0) = 0$ give the weak problem: find u such that

$$a(u,w) = \int_0^L E_fA_fu'w'\,\mathrm{d}x + \int_0^L p_fGuw\,\mathrm{d}x = 0 \tag{11}$$

for every admissible w. The first term represents axial strain energy in the fiber. The second represents the matrix deformation condensed into the distributed bond foundation. Because the foundation term is strictly positive for any nonzero field, the assembled stiffness is symmetric and positive definite even before imposing the essential condition; no rigid-body zero-energy mode exists. The condition $u(L) = \delta$ selects the particular solution rather than removing a singularity.

For a two-node element of length h,

$$u^h = \boldsymbol{N}\boldsymbol{u}_e, \qquad u^{h\prime} = \boldsymbol{B}\boldsymbol{u}_e, \tag{12}$$

where $\boldsymbol{N} = [(1-\xi)/2 \;\; (1+\xi)/2]$ and $\boldsymbol{B} = [-1/h \;\; 1/h]$. The element matrix follows directly from Eq. (11):

$$\boldsymbol{K}_e = \int_{\Omega_e}\boldsymbol{B}^TE_fA_f\boldsymbol{B}\,\mathrm{d}x + \int_{\Omega_e}\boldsymbol{N}^Tp_fG\boldsymbol{N}\,\mathrm{d}x$$
$$= \frac{E_fA_f}{h}\begin{bmatrix}1 & -1\\ -1 & 1\end{bmatrix} + \frac{p_fGh}{6}\begin{bmatrix}2 & 1\\ 1 & 2\end{bmatrix}. \tag{13}$$

Two-point Gauss quadrature integrates both terms exactly. The prescribed displacement is imposed by matrix partitioning, after which F is recovered as the residual at the constrained degree of freedom. Displacement, axial force, and bond stress are evaluated at the Gauss points. For visualization, Gauss-point values are projected to the nodal space through a global L^2 projection.

4.2 Verification measures

The analytical solution is used as an exact reference solution for the same boundary-value problem. The principal normalized errors are

$$
\begin{aligned}
e_F &= \frac{|F_h - F|}{|F|}, \\
e_{L^2} &= \left[\frac{\int_0^L (u_h - u)^2 \,\mathrm{d}x}{\int_0^L u^2 \,\mathrm{d}x} \right]^{1/2}, \\
e_E &= \left[\frac{a(u_h - u, u_h - u)}{a(u,u)} \right]^{1/2}.
\end{aligned} \tag{14}
$$

An analogous relative L^2 norm is used for the axial-force field. Observed orders between consecutive uniform meshes are calculated from $p = \ln(e_i/e_{i+1})/\ln(h_i/h_{i+1})$.

The implementation was subjected to 12 automated tests. They check the published analytical expressions, both boundary conditions, equality between the integrated and closed-form element matrices, matrix symmetry and positive definiteness, free-degree residuals, equality of reaction and integrated interface transfer, linear load scaling, the analytical and discrete energy identities, the L^2 projection, convergence rates, and rejection of imposed displacements beyond s_0. All tests passed. At 80 elements, the equilibrium difference between the reaction and $\int_0^L p_f \tau \,\mathrm{d}x$ is 2.93×10^{-14} N.

Table 3: Summary of code-verification evidence.

Check	Outcome
Analytical expressions and boundary conditions	Numerical precision
Integrated versus closed element matrix	Numerical precision
Symmetry and positive definiteness	Satisfied
Reaction versus integrated bond transfer	2.93×10^{-14} N
Analytical and discrete energy identities	Numerical precision
Expected convergence orders (F, u, N, E)	$(2, 2, 1, 1)$
Automated verification suite	12 of 12 passed

5 Axisymmetric finite element model

The continuum model was created in Abaqus as one axisymmetric part partitioned at $r = r_f$. Elastic steel and matrix sections were assigned to the two regions; the shared topology enforces perfect displacement continuity without a separate cohesive or contact law. The matrix therefore develops its shear deformation explicitly. Neither the effective modulus G nor the strength $\tau_{\max}$ is supplied to this model. The latter is used only to select the comparison displacement s_0 obtained from Model A.

The symmetry axis satisfies $U_1 = 0$. Zhan and Meschke define the reduced displacement relative to the matrix boundary at $r = R$ [1]; setting $U_2 = 0$ on that boundary therefore fixes the same axial reference, while leaving radial motion free avoids suppressing Poisson contraction. The embedded fiber tip remains free and $U_2 = \delta$ is prescribed on the loaded end of the fiber. A static, geometrically linear analysis is performed with four-node bilinear axisymmetric quadrilaterals (CAX4). The reaction is the sum of RF_2 over the loaded fiber edge.

The mesh is structured and graded radially toward the fiber-matrix partition. Axial and radial refinements were evaluated separately to remain below the 1,000-node limit of Abaqus Learning Edition. In the axial family A1–A4, $N_r = 10$ is fixed while N_z increases. In the radial family R1–R4, $N_z = 40$ is fixed while the radial subdivision increases. The convergence measure is

$$
\Delta_i = \frac{|F_i - F_{i-1}|}{|F_i|} \times 100\%. \tag{15}
$$

Because the continuum model is linear, the mesh study was conducted at $\delta = 0.25 s_0 = 5.9455 \times 10^{-5}$ mm and scales directly to s_0.

6 Results

6.1 Verification and convergence of the 1D model

Figure 2 shows monotonic convergence over meshes with 5 to 320 linear elements. At 80 elements, the reaction is 7.001093 N and its relative error is 0.03316%. For the finest mesh, the reaction error decreases to 0.002073%, the displacement L^2 error to 0.003765%, the axial-force L^2 error to 0.64385%, and the energy-norm error to 0.45527%.

The finest observed orders are 2.0000 for the reaction, 1.9999 for the displacement L^2 norm, 0.9999 for the axial-force field, and 1.0000 in the energy norm. These rates match the expected behavior of linear elements for a smooth solution: second-order convergence for displacement and the global reaction and first-order convergence for derivative-based quantities. The agreement of rates, balance, and energy is stronger evidence of a correct implementation than the agreement of one final scalar force alone.

Figure 3 provides the local interpretation. Because $\tau = Gu$, normalized relative displacement and bond stress coincide. Both remain small over most of the embedded length and rise rapidly within a few transfer lengths of the loaded end. Conversely, $N(0) = 0$ and the axial force grows toward F_0 as interfacial shear accumulates. The displacement and bond stress are directly interpolated by the linear element. The axial force is a derivative field and is constant within each element, producing the visible staircase for the 10-element mesh. Refinement recovers the analytical profile.

6.2 Axisymmetric mesh sensitivity

Table 4 shows monotonic directional refinement. At fixed $N_r = 10$, increasing N_z from 40 to 60 changes the reaction by 0.323%, and the subsequent A3-to-A4 change is 0.127%. At fixed $N_z = 40$, the R3-to-R4 radial change is 0.355%. These independent studies support R4 as a practical 984-node reference satisfying the adopted 0.5% engineering criterion. The four-point directional sequences do not support a formal Richardson extrapolation or Grid Convergence Index; asymptotic convergence is therefore not claimed.

The axial strain field in Fig. 4 is consistent with the shear-lag interpretation: deformation is concentrated close to the

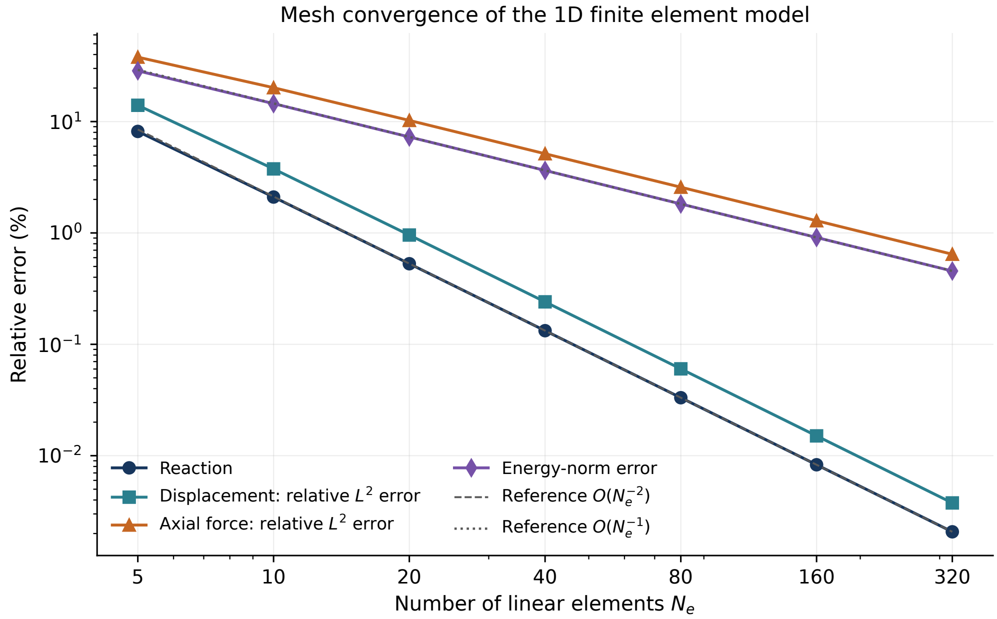

Figure 2: Convergence of the custom one-dimensional finite element model at $\delta = s_0$. Reference slopes are anchored to the finest-mesh errors.

loaded fiber end and spreads into the adjacent matrix. The plot is used qualitatively because the displayed nodal averaging smooths material-side and end effects. Quantitative interface stress comparisons should instead use integration-point S_{12} values along a path on a consistently selected side of the partition.

Table 4: Axial and radial mesh convergence of the CAX4 axisymmetric model at $\delta = 0.25s_0$. The labels R1–R4 denote the radial refinement sequence, not reduced integration.

Mesh	N_z	N_r	Elements	Nodes	F (N)	Δ_i (%)
Axial refinement at fixed radial discretization						
A1	20	10	200	231	2.13691	–
A2	40	10	400	451	2.10764	1.389
A3	60	10	600	671	2.10086	0.323
A4	80	10	800	891	2.09819	0.127
Radial refinement at fixed axial discretization						
R1	40	10	400	451	2.10764	–
R2	40	15	600	656	2.04123	3.253
R3	40	22	880	943	2.01305	1.400
R4	40	23	920	984	2.00593	0.355

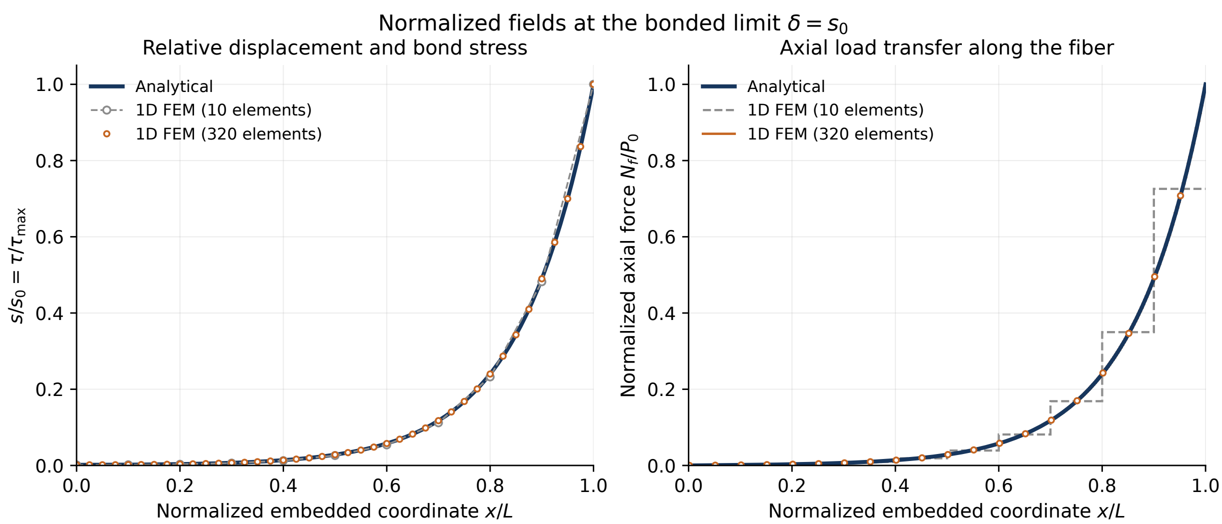

Figure 3: Normalized fields at the bonded limit. Left: relative displacement and bond stress. Right: axial load accumulated along the fiber.

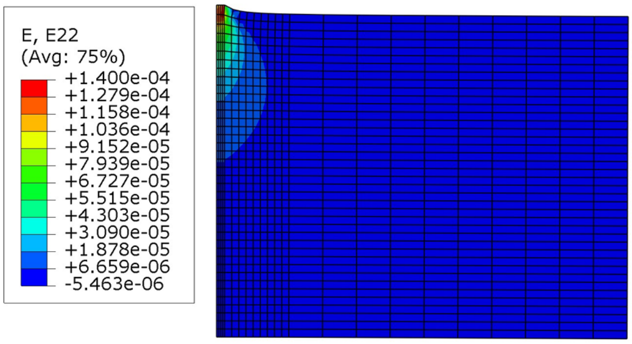

Figure 4: Qualitative nodal-averaged axial strain E_{22} in the practical axisymmetric reference model at the end of the prescribed-displacement step. Nodal averaging smooths material-side and end effects; quantitative interface comparisons should use integration-point S_{12} along a fixed path.

6.3 Cross-model and experimental comparison

Table 5 compares all models at the analytical bonded-limit displacement. Models A and B are essentially coincident: the 80-element force differs from the closed form by 0.033%. The R4 axisymmetric force is 8.02372 N, or 14.645% above the analytical value. A least-squares fit of all exported Abaqus reaction points constrained through the origin gives K = 33738.619 N/mm and $R^2 \approx 1.0000$; deviations are below 10^{-4}% of the end reaction. The difference from Model A is therefore not caused by nonlinear response.

Table 5: Comparison at $\delta = s_0$. Experimental values were digitized from Fig. 4 of Ref. [1].

Model	F (N)	K (kN/mm)	Δ_A (%)	Δ_{exp} (%)
Experiment (digitized)	≈ 6.99	–	–	0
Analytical	6.99877	29.4288	0.000	< 0.2
1D FEM, 80 el.	7.00109	29.4386	0.033	< 0.2
Abaqus R4	8.02372	33.7386	14.645	≈ 14.7

Δ_A is the difference from the analytical solution and Δ_{exp} is the approximate difference from the digitized experiment. The latter is a graphical benchmark, not raw experimental data or a formal uncertainty estimate.

The analytical and 80-element strain energies at s_0, evaluated independently by integration and the discrete quadratic form, are 8.32225×10^{-4} and 8.32500×10^{-4} N mm, respectively. For R4, $U = 9.54101 \times 10^{-4}$ N mm is inferred from the linear identity $U = F\delta/2$; it therefore restates the reaction result rather than providing an independent Abaqus energy check.

Figure 5 places the modeled interval within the complete experimental response. At s_0, the digitized curve gives approximately 7.0 N. The analytical and 1D predictions differ from this graphical estimate by less than 0.2%; however, this difference is below the defensible precision of manual raster digitization and is not a formal validation metric. The axisymmetric result is approximately 14.7% higher. Beyond s_0, the experiment continues nonlinearly to approximately 50 N at 0.0063 mm, while the present models are intentionally terminated. Extrapolating their bonded linear stiffness into that region would have no physical basis.

7 Discussion

7.1 What the agreement of Models A and B proves

The nearly exact overlap of the analytical and 1D curves is expected because both solve Eq. (3) with the same parameters and boundary conditions. Its significance is numerical rather than independent physical confirmation. The closed-form solution exposes implementation errors that a single converged-looking curve might conceal: an incorrect sign in the weak form, a lumped instead of consistent foundation, inaccurate quadrature, or an incorrect reaction recovery would alter the convergence rates, equilibrium, or energy identities. Passing these checks establishes that the custom code is a verified discretization of the adopted shear-lag model.

The local profiles also clarify the physical content of the equations. The first derivative of displacement is the fiber strain, $N/(E_f A_f)$; the increase of N along x equals the accumulated interfacial shear transfer. The length $1/\lambda$ therefore measures how rapidly load can migrate from the fiber into the matrix. The equality $u/s_0 = \tau/\tau_{\max}$ in Fig. 3 is not a general property of pullout. It follows only from the linear bonded law and ceases to hold after damage initiates.

7.2 Interpretation of the axisymmetric stiffness difference

The difference between R4 and Model A remains essentially unchanged over the last accessible refinements and shows no tendency to close toward the reduced solution. It is therefore interpreted, within this range, as model-form discrepancy rather than unresolved Abaqus discretization error. The reduced model condenses the matrix field into G, whereas Model C resolves axial and radial matrix deformation, Poisson coupling, and two-dimensional end fields. The continuum boundary idealization, finite outer boundary, and loaded-end neighborhood may also contribute. Their individual effects are not isolated here.

This distinction also explains why the bond strength has different roles. In Model A, $\tau_{\max}$ is part of the constitutive interface law and defines the end of the bonded solution. In Model C, no strength or damage criterion is present: s_0 is merely a prescribed comparison displacement. The continuum model can generate an interfacial shear field, but it does not "know" that 3.18 MPa should trigger debonding. Local peaks close to the loaded corner may also be mesh-sensitive. A path-based comparison of $S_{12}(x)$ should therefore avoid interpreting a single corner value as a material strength measurement.

7.3 Evidence level and limitations

The experimental comparison is a reproduction of a published benchmark, not an independent validation. The interface parameters in Ref. [1] were determined from the same experimental program, and the curve used here was digitized manually from a raster figure. No formal digitization-uncertainty analysis was performed. The close graphical agreement of Model A with that curve confirms that the published bonded branch and parameters were reproduced consistently; it does not provide new parameter validation.

The study is restricted to a straight, aligned, single fiber,

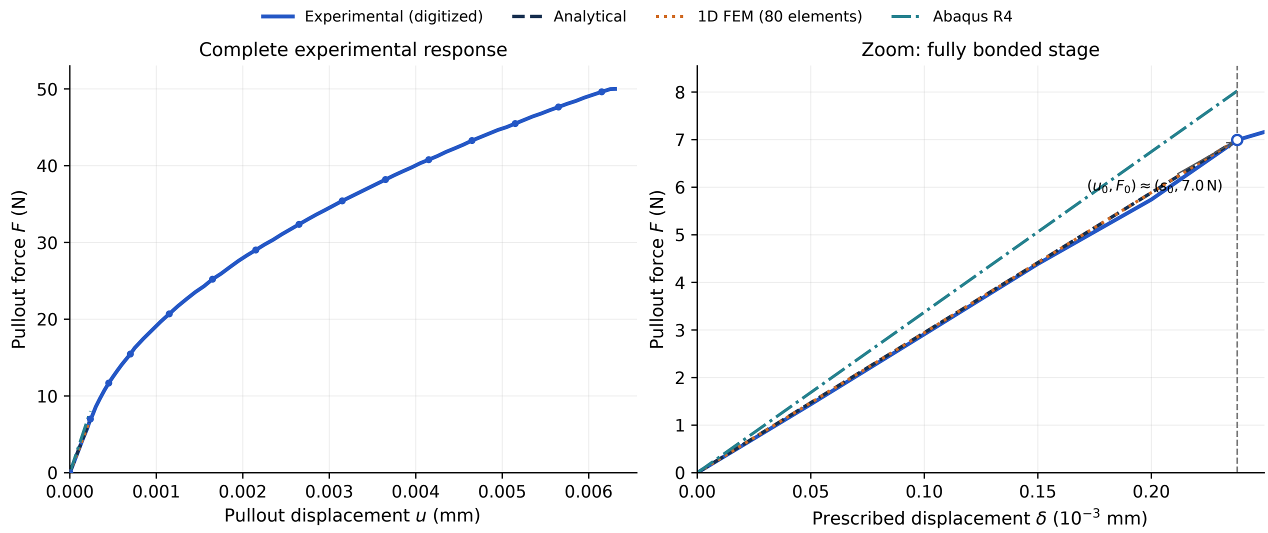

Figure 5: Experimental and numerical pullout responses. The left panel places the modeled interval in the complete digitized curve; the right panel enlarges the fully bonded stage. The experimental curve is an approximate digitization of Fig. 4 in Ref. [1].

small strain, linear elasticity, and the interval $0 \le \delta \le s_0$. It excludes interface damage, residual friction, full extraction, matrix cracking, fiber yielding, inclination, hooks, and fiber-group effects. These mechanisms are central to the subsequent experimental response [1, 2] and to more general discrete or multiscale descriptions [3, 4, 5]. The Abaqus mesh is additionally constrained by the 1,000-node educational limit. Thus, the directional sequences establish the adopted engineering tolerance but not an asymptotic error estimate or formal Grid Convergence Index. A future archive should include the Abaqus input deck and raw history exports. Nevertheless, the reduced scope supplies a transparent baseline for testing nonlinear interface formulations.

8 Conclusions

A three-level hierarchy was constructed for the fully bonded stage of straight steel-fiber pullout. The analytical solution identifies the transfer length, end-of-bond displacement, and exact reference response. The custom 1D formulation converges with the expected second-order rates for reaction and displacement and first-order rates for axial force and energy. Its 80-element reaction error is 0.033%, with equilibrium and energy residuals at numerical precision.

The CAX4 response satisfies the adopted 0.5% criterion in independent directional studies, whose final axial and radial changes are 0.127% and 0.355%, respectively. The 984-node R4 mesh predicts 8.02372 N at s_0, about 14.6% above the analytical force. Its linearity and stabilization support interpreting the residual as a model-form difference within the accessible refinement range; formal asymptotic convergence was not established.

At the same displacement, the analytical and 1D results coincide with the digitized graphical estimate to within its defensible precision. This evidence is limited to the calibrated initial branch. The next model should introduce an explicit traction-slip law with debonding and residual friction and compare integration-point shear stress along the interface, while preserving the verification and mesh-convergence procedures established here.

References

[1] Y. Zhan and G. Meschke, "Analytical model for the pullout behavior of straight and hooked-end steel fibers," *Journal of Engineering Mechanics*, vol. 140, no. 12, 04014091, 2014. doi: 10.1061/(ASCE)EM.1943-7889.0000800.

[2] R. Breitenbücher, G. Meschke, F. Song, and Y. Zhan, "Experimental, analytical and numerical analysis of the pullout behaviour of steel fibres considering different fibre types, inclinations and concrete strengths," *Structural Concrete*, vol. 15, no. 2, pp. 126–135, 2014. doi: 10.1002/suco.201300058.

[3] J. Kang, K. Kim, Y. M. Lim, and J. E. Bolander, "Modeling of fiber-reinforced cement composites: Discrete representation of fiber pullout," *International Journal of Solids and Structures*, vol. 51, pp. 1970–1979, 2014. doi: 10.1016/j.ijsolstr.2014.02.006.

[4] L. A. G. Bitencourt Jr., O. L. Manzoli, T. N. Bittencourt, and F. J. Vecchio, "Numerical modeling of steel fiber reinforced concrete with a discrete and explicit representation of steel fibers," *International Journal of Solids and Structures*, vol. 159, pp. 171–190, 2019. doi: 10.1016/j.ijsolstr.2018.09.028.

[5] P. O. Ribeiro, *Contributions to a Constitutive Model for Ultra-High Performance Fiber-Reinforced Concrete*. Doctoral thesis, São Carlos School of Engineering, University of São Paulo, São Carlos, Brazil, 2023.

AI-assisted preparation

OpenAI ChatGPT was used to support code review, data organization, language revision, and manuscript preparation. The authors remain responsible for the final content.